EUROPEAN ORGANIZATION FOR NUCLEAR RESEARCH

ΛK femtoscopy in Pb-Pb collisions at $\sqrt{s_{\mathrm{NN}}} = 2.76$ TeV

ALICE Collaboration*

Abstract

The first measurements of the scattering parameters of ΛK pairs in all three charge combinations (ΛK^+, ΛK^-, and ΛK_S^0) are presented. The measurements are achieved through a femtoscopic analysis of ΛK correlations in Pb-Pb collisions at $\sqrt{s_{\mathrm{NN}}}$ = 2.76 TeV from ALICE at the LHC. The femtoscopic correlations result from strong final-state interactions, and are fit with a parametrization allowing for both the characterization of the pair emission source and the measurement of the scattering parameters for the particle pairs. Extensive studies with the THERMINATOR 2 event generator allow for the description of the non-femtoscopic background, resulting mainly from collective effects, with unprecedented precision. Furthermore, this model together with HIJING simulations are used to account for contributions from residual correlations induced by feed-down from resonances. The ΛK^+ system exhibits a negative real component of the scattering parameter ($\Re f_0$), while those of the ΛK^- and ΛK_S^0 are positive, although the magnitude of that of the ΛK_S^0 is smaller than that of the ΛK^-. The results suggest an effect arising from different quark-antiquark interactions between the pairs ($s\bar{s}$ in ΛK^+ and $u\bar{u}$ in ΛK^-), or from different net strangeness for each system (S=0 for ΛK^+, and S=−2 for ΛK^-). Finally, the ΛK systems exhibit source radii larger than expected from extrapolation from identical particle femtoscopic studies. This effect is interpreted as resulting from the separation in space-time of the single-particle Λ and K source distributions.

*See Appendix D for the list of collaboration members

1 Introduction

Femtoscopy is an experimental method used to study the space-time characteristic of the particle emit-
ting sources in relativistic particle collisions [1]. With this method, two (or many)-particle relative-
momentum correlation functions are used to connect the final-state momentum distributions to the space-
time distributions of particle emission at freeze-out. The correlation functions are sensitive to quantum
statistics, as well as strong and Coulomb final-state interactions (FSI). Current femtoscopic studies are
able to extract the size, shape, and orientation of the pair emission regions, as well as offering estimations
of the total time to reach kinetic decoupling and the suddenness of particle emission. Non-identical par-
ticle analyses additionally allow for the measurement of the space-time separation of the single particle
source emitting regions. The momentum and species dependence of femtoscopic measurements affirm
the collective nature of the hot and dense matter created in heavy-ion collisions.

In addition to characterizing the source region, femtoscopy offers a unique environment in which to mea-
sure nuclear scattering parameters, many of which are difficult, if not impossible, to measure otherwise.
This aspect of femtoscopy is the focal point of the present analysis. In this analysis, Λ-K pairs are stud-
ied, in which at least one particle is electrically neutral. Quantum statistics and the Coulomb interaction
do not contribute, offering a clear signal from the strong interaction.

Calculations within Quantum Chromodynamics (QCD), the theory of the strong interaction, are notori-
ously difficult except in select regimes of weak coupling, where perturbative methods may be applied.
The ΛK analysis presented offers low energy QCD measurements, which fall into the non-perturbative
regime of QCD. Therefore, the ΛK measurements not only give insight into the strong interaction, they
will also help guide future QCD calculations. This study is also particularly interesting, as the ΛK scatter-
ing parameters are not known, and therefore the behavior of the system cannot be predicted beforehand.
Scattering parameters for similar systems are also very limited; past studies of kaon-proton scattering
revealed the strong force is attractive in the K^-p interaction, and repulsive in that of the K^+p [2–4].

This paper presents the first measurements of the scattering parameters of ΛK pairs in all three charge
combinations (ΛK^+, ΛK^-, and ΛK_S^0). The scattering parameters, along with pair emission source sizes,
are extracted with a femtoscopic analysis of ΛK correlations in Pb-Pb collisions at $\sqrt{s_{NN}} = 2.76$ TeV from
the ALICE experiment at the LHC. These correlations result from strong final-state interactions, and are
fit with a parametrization by Lednický and Lyuboshitz [5]. Extensive studies with the THERMINATOR 2
event generator are performed to account for both non-femtoscopic backgrounds, as well as contributions
from residual correlations induced by feed-down from resonances.

The organization of this paper is as follows. In Sec. 2 the data selection methods are briefly discussed.
In Sec. 3 the analysis techniques utilized in this study are presented. Here, the two particle correlation
function is introduced, as well as the theoretical models with which the data are fit. This section also
includes descriptions of the handling of residual correlations, corrections accounting for finite track
momentum resolution, treatment of the non-femtoscopic background, as well as a brief description of
the systematic uncertainties estimation. The final results are presented in Sec. 4, and concluding remarks
are given in Sec. 5. Appendix A demonstrates an alternate approach to forming correlation functions,
whose purpose here is to help eliminate the non-femtoscopic background. Appendix B discusses the
procedure needed to generate fit functions when both the strong and Coulomb interactions are present.
In Appendix C, the THERMINATOR 2 event generator is used to demonstrate the effect of increasing
the source offset in the "out" direction (μ_{out}) on a one-dimensional femtoscopic fit. Throughout the text,
the pair name is used as shorthand for the pair-conjugate system, which are found to be consistent (e.g.
ΛK_S^0, $\Lambda K^+ \oplus \bar{\Lambda} K^-$ is simply ΛK^+).

2 Data Analysis

The dataset analyzed is from Pb-Pb collisions at $\sqrt{s_{NN}}$ = 2.76 TeV at the LHC measured by the ALICE detector [6] in 2011. Approximately 40 million combined central, semi-central, and minimum bias events were analyzed. The events were classified according to their centrality determined using the measured amplitudes in the V0 detectors [7]. In order for an event to be included in the analysis, the z-position of the reconstructed event vertex must be within 10 cm of the center of the ALICE detector, and the event must contain at least one particle of each type from the pair of interest (e.g. for ΛK_S^0 analysis, an accepted event must contain at least one Λ and at least one K_S^0).

Charged particle tracking was performed using the Time Projection Chamber (TPC) [8] and the Inner Tracking System [9]. The ITS allows for high spatial resolution in determining the primary (collision) vertex. The determination of the momenta of the tracks was performed using tracks reconstructed with the TPC only and constrained to the primary vertex. A minimum requirement of 80 reconstructed TPC clusters was imposed, the purpose of which is to ensure both the quality of the track and good p_T resolution at large momenta, as well as to remove fake tracks.

Particle identification (PID) for reconstructed tracks was carried out using both the TPC and Time-of-Flight (TOF) detector [10, 11] in the pseudorapidity range $|\eta| < 0.8$. For TPC PID, a parametrized Bethe-Bloch formula was used to calculate the specific energy loss $\langle dE/dx \rangle$ in the detector expected for a particle with a given mass and momentum. For TOF PID, the particle mass was used to calculate the expected time-of-flight as a function of track length and momentum. For each PID method, a value (N_σ) was assigned to each track denoting the number of standard deviations between the measured track information and calculated values. This procedure was repeated for four "particle species hypotheses"— electron, pion, kaon, and proton—, and for each hypothesis a different N_σ value was obtained per detector.

2.1 $K^\pm$ selection

The single-particle selection criteria used to select charged kaon candidates are summarized in Table 1. $K^\pm$ track detection utilized both TPC and TOF detectors, and tracks within the range $0.14 < p_T < 1.5$ GeV/c were accepted. To reduce the number of secondaries (e.g. charged particles produced in the detector material, particles from weak decays, etc.) in the sample, a maximum cut is established on the distance-of-closest-approach (DCA) of the track to the primary vertex. This restriction is realized by imposing a DCA cut in both the transverse and beam directions.

PID was performed using both the TPC and TOF detectors via the N_σ method. The N_σ cuts become tighter with increasing momentum to reduce contamination within the samples, as the $K^\pm$ signals begin to overlap more significantly with those from other particles, particularly $e^\pm$ and $\pi^\pm$. Additional methods are included to reduce the contamination in the $K^\pm$ samples from the electrons and pions. The specifics for these cuts are contained in Table 1. The purity of the $K^\pm$ collections, $P_{K^\pm}$, was estimated to be approximately 97% from a Monte-Carlo (MC) study based on HIJING [12] simulations using GEANT3 [13] to model particle transport through the ALICE detectors. For a more detailed estimate of the $K^\pm$ purity from an analysis employing similar cuts, see Ref. [14].

2.2 V^0 selection

$\Lambda(\bar{\Lambda})$ and K_S^0 particles are reconstructed through their weak decays: $\Lambda \rightarrow p\pi^-$ ($\bar{\Lambda} \rightarrow \pi^+\bar{p}$) and $K_S^0 \rightarrow \pi^+\pi^-$. The obtained candidates are denominated as V^0 particles. The main cuts used are shown in Tables 2 and 3.

Aside from typical kinematic and PID cuts (using TPC and TOF detectors), the daughter tracks are also exposed to a minimum cut on their impact parameter with respect to the primary vertex. The decay vertex of the V^0 is assumed to be the point of closest approach between the daughter tracks. To help ensure

3

$K^\pm$ **selection**			
Transverse momentum p_T			$0.14 < p_T < 1.5$ GeV/c
$|\eta|$			< 0.8
Transverse DCA to primary vertex			< 2.4 cm
Longitudinal DCA to primary vertex			< 3.0 cm
TPC and TOF N_σ Cuts			
$p < 0.4$ GeV/c			$N_{\sigma K, \text{TPC}} < 2$
$0.4 \leq p < 0.45$ GeV/c			$N_{\sigma K, \text{TPC}} < 1$
$0.45 \leq p < 0.80$ GeV/c			$N_{\sigma K, \text{TPC}} < 3$ $N_{\sigma K, \text{TOF}} < 2$
$0.80 \leq p < 1.0$ GeV/c			$N_{\sigma K, \text{TPC}} < 3$ $N_{\sigma K, \text{TOF}} < 1.5$
$p \geq 1.0$ GeV/c			$N_{\sigma K, \text{TPC}} < 3$ $N_{\sigma K, \text{TOF}} < 1$
Electron Rejection: Reject if all satisfied			$N_{\sigma e^-, \text{TPC}} < 3$ $N_{\sigma e^-, \text{TPC}} < N_{\sigma K^\pm, \text{TPC}}$ $N_{\sigma e^-, \text{TOF}} < N_{\sigma K^\pm, \text{TOF}}$
Pion Rejection: Reject if:			
$p < 0.65$ GeV/c	TOF and TPC available		$N_{\sigma\pi, \text{TPC}} < 3$ $N_{\sigma\pi, \text{TOF}} < 3$
	Only TPC available	$p < 0.5$ GeV/c	$N_{\sigma\pi, \text{TPC}} < 3$
		$0.5 \leq p < 0.65$ GeV/c	$N_{\sigma\pi, \text{TPC}} < 2$
$0.65 \leq p < 1.5$ GeV/c			$N_{\sigma\pi, \text{TPC}} < 5$ $N_{\sigma\pi, \text{TOF}} < 3$
$p \geq 1.5$ GeV/c			$N_{\sigma\pi, \text{TPC}} < 5$ $N_{\sigma\pi, \text{TOF}} < 2$

Table 1: $K^\pm$ selection

4

111   quality, a maximum value cut is demanded on the distance-of-closest-approach between the daughters
112   (DCA V^0 Daughters). The positive and negative daughter tracks are combined to form the V^0 candidate,
113   the momentum of which is simply the sum of the momenta of the daughters (calculated at the DCA).

114   To select primary candidates, each V^0 is exposed to a maximum cut on its impact parameter with respect
115   to the primary vertex. Furthermore, a selection is imposed on the pointing angle, θ_{pa}, between the V^0
116   momentum and the vector pointing from the primary vertex to the secondary V^0 decay vertex, which is
117   achieved by appointing a minimum value on $\cos(\theta_{pa})$ ("Cosine of pointing angle" in Tables 2 and 3).

118   In order to remove the contamination to the $\Lambda(\bar{\Lambda})$ and K_S^0 samples due to misidentification of the protons
119   and pions for each V^0, the mass assuming different identities (Λ, $\bar{\Lambda}$, K_S^0)[1] is calculated and utilized in
120   a set of misidentification cuts. For $\Lambda(\bar{\Lambda})$ selection, a candidate is assumed to be misidentified and is
121   rejected if all of the following criteria are satisfied:

122   1. $\left| m_{\mathrm{inv},\,K_S^0\,\mathrm{hyp.}} - m_{\mathrm{PDG},\,K_S^0} \right| < 9.0\ \mathrm{MeV}/c^2$

123   2. The daughter particles pass daughter cuts intended for K_S^0 reconstruction

124   3. $\left| m_{\mathrm{inv},\,K_S^0\,\mathrm{hyp.}} - m_{\mathrm{PDG},\,K_S^0} \right| < \left| m_{\mathrm{inv},\,\Lambda(\bar{\Lambda})\,\mathrm{hyp.}} - m_{\mathrm{PDG},\,\Lambda(\bar{\Lambda})} \right|$

125   Similarly, for K_S^0 selection, a candidate is rejected if all of the following criteria are satisfied for the Λ
126   case, or for the $\bar{\Lambda}$ case:

127   1. $\left| m_{\mathrm{inv},\,\Lambda(\bar{\Lambda})\,\mathrm{hyp.}} - m_{\mathrm{PDG},\,\Lambda(\bar{\Lambda})} \right| < 9.0\ \mathrm{MeV}/c^2$

128   2. The daughter particles pass daughter cuts intended for $\Lambda(\bar{\Lambda})$ reconstruction

129   3. $\left| m_{\mathrm{inv},\,\Lambda(\bar{\Lambda})\,\mathrm{hyp.}} - m_{\mathrm{PDG},\,\Lambda(\bar{\Lambda})} \right| < \left| m_{\mathrm{inv},\,K_S^0\,\mathrm{hyp.}} - m_{\mathrm{PDG},\,K_S^0} \right|$

130   A final cut on the invariant mass (m_{inv}) is applied to enhance the purity. These cuts are shown in Tables
131   2 and 3. Finally, to avoid any auto-correlation effects, all V^0 candidates are ensured to have unique
132   daughters. If a daughter is found to be shared between V^0 candidates, only the candidate with the
133   smallest DCA to the primary vertex is kept. The resulting invariant mass distributions for Λ and K_S^0
134   collections in the 0–10% centrality bin are shown in Figure 1. For the purity estimations, the background
135   signal is estimated by fitting the m_{inv} distribution outside of the mass peak and assuming the distribution
136   to continue smoothly within the mass peak. The Λ and $\bar{\Lambda}$ purities are estimated to be $P_{\Lambda(\bar{\Lambda})} \approx 95\%$, and
137   that of the K_S^0 is $P_{K_S^0} \approx 98\%$.

2.3   Pair Construction

139   In order to reduce the contamination to the two-particle correlations due to pairs sharing daughters and to
140   split or merged tracks, two main pair cuts are applied: a shared daughter cut, and an average separation
141   cut. The purpose of the shared daughter cut is to ensure the first particle in the pair is unique from the
142   second. For pairs formed of two V^0s (i.e. ΛK_S^0), this cut is implemented by removing all pairs which
143   share a daughter. For a pair formed of a single V^0 and a charged track (i.e. $\Lambda K^{\pm}$), the cut removes all
144   pairs in which the charged track is also claimed as a daughter of the V^0.

---

[1] For the misidentification cuts, the mass assuming K_S^0 hypothesis ($m_{\mathrm{inv},\,K_S^0\,\mathrm{hyp.}}$) is calculated assuming $\pi^+\pi^-$ daughters, the mass assuming Λ hypothesis ($m_{\mathrm{inv},\,\Lambda\,\mathrm{hyp.}}$) is calculated assuming $p\pi^-$ daughters, and the mass assuming $\bar{\Lambda}$ hypothesis ($m_{\mathrm{inv},\,\bar{\Lambda}\,\mathrm{hyp.}}$) is calculated assuming $\bar{p}\pi^+$ daughters. Additionally, $m_{\mathrm{PDG},\,K_S^0}$ and $m_{\mathrm{PDG},\,\Lambda(\bar{\Lambda})}$ denote the particle masses of the K_S^0 and $\Lambda(\bar{\Lambda})$, respectively, as recorded by the Particle Data Group [15].

Λ selection	
Transverse momentum p_T	> 0.4 GeV/c
$|\eta|$	< 0.8
Invariant mass	$|m_{p\pi} - m_{PDG}| < 3.8$ MeV/c^2
DCA to primary vertex	< 0.5 cm
Cosine of pointing angle	> 0.9993
Decay Length	< 60 cm
Daughter Cuts (π and p)	
$|\eta|$	< 0.8
DCA πp Daughters	< 0.4 cm
π-specific cuts	
p_T	> 0.16 GeV/c
DCA to primary vertex	> 0.3 cm
TPC and TOF N_σ Cuts	

$p < 0.5$ GeV/c		$N_{\sigma_{TPC}} < 3$
$p \geq 0.5$ GeV/c	TOF & TPC available	$N_{\sigma_{TPC}} < 3$
		$N_{\sigma_{TOF}} < 3$
	Only TPC available	$N_{\sigma_{TPC}} < 3$

p-specific cuts	
p_T	> 0.5(p) [$0.3(\bar{p})$] GeV/c
DCA to primary vertex	> 0.1 cm
TPC and TOF N_σ Cuts	

$p < 0.8$ GeV/c		$N_{\sigma_{TPC}} < 3$
$p \geq 0.8$ GeV/c	TOF & TPC available	$N_{\sigma_{TPC}} < 3$
		$N_{\sigma_{TOF}} < 3$
	Only TPC available	$N_{\sigma_{TPC}} < 3$

Table 2: Λ selection

K_S^0 selection	
Transverse momentum p_T	> 0.2 GeV/c
$|\eta|$	< 0.8
Invariant mass	$0.480 < m_{\pi^+\pi^-} < 0.515$ GeV/c^2
DCA to primary vertex	< 0.3 cm
Cosine of pointing angle	> 0.9993
Decay Length	< 30 cm
$\pi^\pm$ Daughter Cuts	
p_T	> 0.15 GeV/c
$|\eta|$	< 0.8
DCA $\pi^+\pi^-$ Daughters	< 0.3 cm
DCA to primary vertex	> 0.3 cm
TPC and TOF N_σ Cuts	

$p < 0.5$ GeV/c		$N_{\sigma_{TPC}} < 3$
$p \geq 0.5$ GeV/c	TOF & TPC available	$N_{\sigma_{TPC}} < 3$
		$N_{\sigma_{TOF}} < 3$
	Only TPC available	$N_{\sigma_{TPC}} < 3$

Table 3: K_S^0 selection

6

(a) $p\pi^-$ invariant mass distribution where the Λ peak is seen. (b) $\pi^+\pi^-$ invariant mass distribution where the K^0_S peak is seen.

Fig. 1: (Color online) Invariant mass (m_{inv}) distribution of $p\pi^+$ pairs showing the Λ peak 1(a), and of $\pi^+\pi^-$ pairs showing the K^0_S peak 1(b), for V^0 candidates. The bottom panels are zoomed to show the background with fit. The vertical dashed lines represent the m_{inv} cuts used in the analyses, the vertical dotted lines delineate the region over which the background was fit, and the dash-dotted line shows the background fit.

The purpose of the average separation cut is to remove splitting and merging effects, and it is employed in the following way. The average separation between two tracks is calculated using their spatial separation as determined at several points throughout the TPC (every 20 cm radially from 85 cm to 245 cm). For the ΛK^0_S analysis, which involves two V^0 particles, a minimum average separation cut of 6 cm between the like-charge daughters in the pairs is imposed (for example, between the p daughter of the Λ and the π^+ daughter of the K^0_S). For the $\Lambda K^\pm$ analyses, a minimum average separation cut of 8 cm is enforced between the $K^\pm$ and the Λ daughter sharing the same charge (for example, in the ΛK^+ analysis, between the p daughter of the Λ and the K^+). The cut values used coincide with the values at which the average separation correlation functions stabilize to unity, signifying the splitting and merging effects are no longer abundant. These effects between oppositely charged tracks were found to be negligible, therefore no cuts on unlike-charge tracks are imposed.

3 Analysis Methods

3.1 Correlation Function

Two-particle correlation functions are built as the ratio of the covariant two-particle and single-particle spectra:

$$C^{ab}(\vec{p}_a, \vec{p}_b) = \frac{E_a E_b \frac{dN^{ab}}{d^3 p_a d^3 p_b}}{\left(E_a \frac{dN^a}{d^3 p_a}\right)\left(E_b \frac{dN^b}{d^3 p_b}\right)} \tag{1}$$

This may be expressed theoretically as in the Koonin-Pratt equation [16, 17]:

$$C(\mathbf{k}^*) = \int S_{\mathbf{P}}(\mathbf{r}^*)|\Psi_{\mathbf{k}^*}(\mathbf{r}^*)|^2 d^3\mathbf{r}^* \tag{2}$$

where $\mathbf{k}^*$ is the relative momentum of the pair (defined as $\mathbf{k}^* = \frac{1}{2}|\mathbf{p}_1^* - \mathbf{p}_2^*|$, where $\mathbf{p}_1^*$ and $\mathbf{p}_2^*$ are the momenta of the two particles) in the pair rest frame (PRF), $\mathbf{r}^*$ is the relative separation in the same frame, $\mathbf{P}$ is the total pair momentum, $S_{\mathbf{P}}(\mathbf{r}^*)$ is the pair source distribution, and $\Psi_{\mathbf{k}^*}(\mathbf{r}^*)$ is the two-particle wave-function. Within the $|\Psi|^2$ term is contained the particle interaction information, and therefore the scattering parameters.

166 In practice, the correlation function is formed experimentally as:

$$C(k^*) = \mathcal{N} \frac{A(k^*)}{B(k^*)} \tag{3}$$

167 where $A(k^*)$ is the signal distribution, $B(k^*)$ is the reference distribution, and $\mathcal{N}$ is a normalization
168 parameter. $B(k^*)$ is used to divide out the phase-space effects, leaving only the femtoscopic effects in the
169 correlation function. The normalization parameter is chosen such that the mean value of the correlation
170 function equals unity for $k^* \in [0.32, 0.4]$ GeV/c.

171 In practice, $A(k^*)$ is constructed by binning in k^* pairs from the same event. Typically, $B(k^*)$ is obtained
172 by forming mixed-event pairs [18], i.e. particles from a given event are paired with particles from N_{mix}
173 other events, and these pairs are then binned in k^*. Other techniques exist; most notably, one may use
174 same-event pairs after rotating one particle in the pair by $180°$ in the transverse plane (see Sec. 3.5 and
175 App. A for more details). For this analysis, the typical mixed-event method is utilized, and each event
176 is mixed with $N_{mix} = 5$ others for the reference distribution construction. In order to mix only similar
177 events, events are binned both in primary vertex location (2 cm bin width) and in centrality (5% bin
178 width), and only events within a given bin are mixed; i.e. only events of like centrality and of like
179 primary vertex location are mixed.

180 This analysis presents correlation functions for three centrality bins (0–10%, 10–30%, and 30–50%),
181 and is pair transverse momentum ($k_T = \frac{1}{2}|\mathbf{p}_{T,1} + \mathbf{p}_{T,2}|$) integrated (i.e. not binned in k_T) due to limited
182 statistics. The k_T-dependence of the three ΛK combinations is comparable, so an integrated analysis is
183 acceptable. The correlation functions are constructed separately for the two magnetic field configurations
184 ($++$ and $--$). These are kept separate during the fitting process, and are combined using a weighted
185 average when plotting, where the weight is the number of numerator pairs in the normalization range.

3.2 Modeling the correlation function

187 In the absence of the Coulomb interaction, the correlation function can be described analytically with a
188 model derived by Lednický and Lyuboshitz [5]. Within the model, the (non-symmetrized) two-particle
189 wave function is expressed as a superposition of a plane wave and diverging spherical wave, and the
190 complex scattering amplitude, $f^S(k^*)$, is evaluated via the effective range approximation

$$f^S(k^*) = \left(\frac{1}{f_0^S} + \frac{1}{2} d_0^S k^{*2} - ik^* \right)^{-1} \tag{4}$$

191 where f_0^S is the complex s-wave scattering length, d_0^S is the effective range of the interaction, and S
192 denotes the total spin of the particular pair. A spherically symmetric Gaussian distribution with radius
193 R_{inv} is assumed for the pair emission source in the PRF. With these assumptions, utilizing the Koonin-
194 Pratt equation (Eq. 2), the correlation function for non-identical particle pairs with at least one uncharged
195 member is given by [5]

$$C(k^*)_{\text{Lednický}} = 1 + \sum_S \rho_S \left[\frac{1}{2} \left| \frac{f^S(k^*)}{R_{inv}} \right|^2 \left(1 - \frac{d_0^S}{2\sqrt{\pi} R_{inv}} \right) + \frac{2\Re f^S(k^*)}{\sqrt{\pi} R_{inv}} F_1(2k^* R_{inv}) - \frac{\Im f^S(k^*)}{R_{inv}} F_2(2k^* R_{inv}) \right] \tag{5}$$

196 where $\Re f^S(k^*)$ and $\Im f^S(k^*)$ denote the real and imaginary parts of the complex scattering length, re-
197 spectively, and F_1 and F_2 are the analytic functions. The weight factor, ρ_S is the normalized emission
198 probability for a state of total spin S; in the assumed case of unpolarized emission, $\rho_S = (2S+1)/[(2j_1 +
199 1)(2j_2 + 1)]$, where $j_{1,2}$ are the spins of the particles in the pair. The Λ hyperon is spin-1/2 and K mesons
200 are spin-0, so the ΛK system only has one possible total spin state S, and therefore $C(k^*)$ in Eq. 5 has
201 only a single term. In the following, the S superscript is dropped from all scattering parameters.

3.3 Residual Correlations

The purpose of this analysis is study the interaction and scale of the emitting source of the primary ΛK pairs. However, in practice some of the selected particles originate as decay products from other resonances, and some of the final pairs contain a misidentified member. In both cases, these contribute to the finally observed correlation function, and obscure its relation to the primary ΛK system. The contributions from fake pairs, which contain at least one misidentified member, are assumed to average to unity, in which case they simply attenuate the femtoscopic signal. Those pairs whose members originate as daughters from resonances carry information about the parent system. In effect, the correlation between the parents will be visible, although smeared out, in the daughters' signal. This is termed a residual correlation resulting from feed-down. In this analysis, the main source of redidual correlations results from Λ hyperons which have decayed from Σ^0, Ξ^0, and Ξ^- parents.

The finally measured correlation function is a combination of the genuine ΛK correlation with contributions from residual feed-down and misidentified particles

$$C_{\mathrm{measured}}(k^*_{\Lambda\mathrm{K}}) = 1 + \lambda'_{\Lambda\mathrm{K}}[C_{\Lambda\mathrm{K}}(k^*_{\Lambda\mathrm{K}}) - 1] + \sum_{ij} \lambda'_{ij}[C_{ij}(k^*_{\Lambda\mathrm{K}}) - 1]$$

$$\lambda'_{ij} = \lambda_{\mathrm{Fit}}\lambda_{ij}$$

$$\sum_{ij} \lambda'_{ij} = \lambda_{\mathrm{Fit}} \sum_{ij} \lambda_{ij} = \lambda_{\mathrm{Fit}} \tag{6}$$

where the ΛK term represents the genuine ΛK correlation, and the ij terms denote the contributions from residual feed-down and possible impurities. More specifically, $C_{ij}(k^*_{\Lambda\mathrm{K}})$ is the correlation function between parents of particle species i and j, expressed in terms of the relative momentum of the observed daughter ΛK pairs. The λ_{ij} parameters serve as weights dictating the relative strength of each component's contribution to the observed signal, and are normalized to unity (i.e. $\sum_{ij} \lambda_{ij} = 1$, where ij includes also the primary ΛK component). The individual λ_{ij} are fixed (and whose values can be found in Table 4), but the parameter λ_{Fit} is left free. The λ_{Fit} parameter serves as an common factor shared by all contributors, as shown in Eq. 6.

In order to obtain the parent correlation function expressed in the relative momentum of the daughter pair, one must use a transform matrix. The transform matrix describes the decay kinematics of the parent system into the daughter, and maps the k^* of the parent pair onto that of the daughter. Using this matrix, the transformed residual correlation function can be obtained:

$$C_{ij}(k^*_{\Lambda\mathrm{K}}) \equiv \frac{\sum_{k^*_{ij}} C_{ij}\left(k^*_{ij}\right) T\left(k^*_{ij}, k^*_{\Lambda\mathrm{K}}\right)}{\sum_{k^*_{ij}} T\left(k^*_{ij}, k^*_{\Lambda\mathrm{K}}\right)} \tag{7}$$

The transform matrix is generated with the THERMINATOR 2 [19] simulation. It is formed for a given parent pair, ij, by taking all ΛK pairs originating from ij, calculating the relative momentum of the parents (k^*_{ij}) and daughters ($k^*_{\Lambda\mathrm{K}}$), and filling a two-dimensional histogram with the values. The transform matrix is essentially an unnormalized probability distribution mapping the k^* of the parent pair to that of the daughter pair when one or both parents decay.

Femtoscopic analyses are sensitive to the pair emission structure at kinetic freeze-out. Therefore, in the eyes of femtoscopy, any particle born from a resonance decay before last rescattering is seen as primary. The THERMINATOR 2 simulation shows that, aside from primaries, the Λ hyperons and K mesons decay from a large number of resonances ($\sim$50 Λ parent species, and $\sim$70 K parent species), and the most significant contributing pair systems are $\Sigma^0\mathrm{K}$, $\Xi^-\mathrm{K}$, $\Xi^0\mathrm{K}$, $\Sigma^{*+}\mathrm{K}$, $\Sigma^{*-}\mathrm{K}$, $\Sigma^{*0}\mathrm{K}$, $\Lambda\mathrm{K}^*$, $\Sigma^0\mathrm{K}^*$, $\Xi^-\mathrm{K}^*$, and $\Xi^0\mathrm{K}^*$. However, the simulation does not include a hadronic rescattering phase, and not all of the aforementioned pair systems will survive until kinetic freeze-out. The systems resulting from

9

ΛK⁺		$\bar{\Lambda}$K⁻		ΛK⁻		$\bar{\Lambda}$K⁺	
Source	**λ value**	**Source**	**λ value**	**Source**	**λ value**	**Source**	**λ value**
Primary	0.527	Primary	0.526	Primary	0.526	Primary	0.527
Σ^0K⁺	0.111	$\bar{\Sigma}^0$K⁻	0.110	Σ^0K⁻	0.110	$\bar{\Sigma}^0$K⁺	0.111
Ξ^0K⁺	0.039	$\bar{\Xi}^0$K⁻	0.035	Ξ^0K⁻	0.038	$\bar{\Xi}^0$K⁺	0.036
Ξ^-K⁺	0.050	$\bar{\Xi}^+$K⁻	0.046	Ξ^-K⁻	0.050	$\bar{\Xi}^+$K⁺	0.046
Other	0.226	Other	0.235	Other	0.228	Other	0.233
Fakes	0.048	Fakes	0.048	Fakes	0.048	Fakes	0.048

ΛK$_S^0$		$\bar{\Lambda}$K$_S^0$	
Pair System	**λ value**	**Pair System**	**λ value**
Primary	0.543	Primary	0.544
Σ^0K$_S^0$	0.120	$\bar{\Sigma}^0$K$_S^0$	0.120
Ξ^0K$_S^0$	0.042	$\bar{\Xi}^0$K$_S^0$	0.039
Ξ^-K$_S^0$	0.054	$\bar{\Xi}^+$K$_S^0$	0.050
Other	0.194	Other	0.199
Fakes	0.048	Fakes	0.048

Table 4: λ values for the individual components of the ΛK correlation functions.

electromagnetic or weak decays (Σ^0, Ξ^-, and Ξ^0) will survive long after kinetic freeze-out, and will contribute residual signals to the ΛK correlation functions. The majority of the remaining contributors decay via the strong interaction with proper decay lengths less than a few fm, and whose daughters should always be considered primary. The proper decay length of the parent is used to judge whether or not the daughter is treated as primary. A decay product is considered primary if its parent has a proper decay length of $c\tau < 10$ fm. In order for a pair to be considered primary, both particles in the pair must be considered primary. If either parent has $\tau > \tau_{\max}$, the daughter pair contributes to the "Other" category when calculating λ parameters. For this hodgepodge of pair systems, all with different two-particle interactions and single-particle source distributions, we assume the net correlation effect averages to unity. Residual contributions from Σ^0, Ξ^0, Ξ^- are accounted for in the fit.

As previously stated, the λ parameters dictate the strength of the parent contribution to the daughter pair. Therefore, the λ parameter for parent system ij can be estimated as the total number of ΛK pairs in our experimental sample originating from ij (N_{ij}) divided by the total number of ΛK pairs (N_{Total}). The number of ΛK pairs originating from each source involves not only the raw yields for each, but also the corresponding experimental reconstruction efficiencies. The reconstruction efficiencies (RE_{ij}) are estimated with MC HIJING data, which has been run through GEANT to simulate the detector response. HIJING events are generated from a superposition of PYTHIA p-p collisions, and lack the strangeness saturation of a fully thermalized medium. As a result, HIJING is unreliable in providing the yields needed for this analysis, and, instead, the yields are estimated with the THERMINATOR 2 simulation (N_{ij}^{THERM}). The λ parameters are then estimated as

$$\lambda_{ij} = \frac{N_{ij}}{N_{\text{Total}}} = \frac{N_{ij}^{THERM} RE_{ij}^{HIJING}}{\sum_{\alpha\beta} N_{\alpha\beta}^{THERM} RE_{\alpha\beta}^{HIJING}} \tag{8}$$

The λ values used can be found in Table 4, which also included values for "Other" and "Fakes". The "Other" category contains pairs which are not considered primary, and which do not originate from the

261 residual contributors accounted for in the fit. The "Fakes" category represents pairs that are mistakenly
262 identified as ΛK. To estimate this λ_{Fakes} value, the number of fake pairs is assumed to be equal to the
263 total number of simulated pairs multiplied by $(1 - PP_{\Lambda K})/PP_{\Lambda K}$, where $PP_{\Lambda K}$ is the ΛK pair purity,
264 estimated as the product of the two single-particle purities ($PP_{\Lambda K} = P_{\Lambda}P_{K}$). More simply, this amounts
265 to $\lambda_{\text{Fakes}} = 1.0 - PP_{\Lambda K}$. For both of these contributors ("Other" and "Fakes"), it is assumed that these
266 correlations average to unity, and therefore do not contribute to the final correlation function.

267 In practice, the contribution of a parent system (e.g. $\Sigma^{0}K^{+}$) to the daughter correlation function (e.g.
268 ΛK^{+}) is determined by modeling the parent system's correlation function and running it through the
269 appropriate transform matrix. Since the interactions between these particles are not known, all residual
270 pairs are assumed to have the same source size as the daughter pair. Furthermore, Coulomb-neutral
271 residual pairs are assumed to share the same scattering parameters as the daughter pair. Therefore, for
272 Coulomb-neutral pairs, such as $\Sigma^{0}K$, and $\Xi^{0}K$, $C_{ij}(k^{*}_{ij})$ is calculated from Eq. 5; $C_{ij}(k^{*}_{\Lambda K})$ is then obtained
273 by transforming $C_{ij}(k^{*}_{ij})$ with Eq. 7, using the appropriate transform matrix.

274 When modeling $\Xi^{-}K^{\pm}$ residual correlations, the experimental $\Xi^{-}K^{\pm}$ data is used. Consistent results are
275 found when modeling the $\Xi^{-}K^{\pm}$ system, in which the the strong interaction is assumed to be negligible,
276 and the parent correlation is generated assuming a Coulomb-only scenario (see Appendix B for more
277 details). This approximation is well justified here as a Coulomb-only description of the system describes,
278 reasonably well, the broad features of the correlation.

3.4 Momentum Resolution Corrections

280 Finite track momentum resolution causes the reconstructed momentum of a particle to smear around the
281 true value. This, of course, also holds true for V^{0} particles. The effect is propagated up to the pairs
282 of interest, which causes the reconstructed relative momentum (k^{*}_{Rec}) to differ from the true momentum
283 (k^{*}_{True}). The effects of finite momentum resolution are accounted for through the use of a response matrix
284 generated with MC HIJING data. With this approach, the resolution correction is applied on-the-fly
285 during the fitting process by propagating the theoretical (fit) correlation function through the response
286 matrix, according to

$$C_{\text{fit}}(k^{*}_{\text{Rec}}) = \frac{\sum\limits_{k^{*}_{\text{True}}} M_{k^{*}_{\text{Rec}},k^{*}_{\text{True}}} C_{\text{fit}}(k^{*}_{\text{True}})}{\sum\limits_{k^{*}_{\text{True}}} M_{k^{*}_{\text{Rec}},k^{*}_{\text{True}}}} \tag{9}$$

287 where $M_{k^{*}_{\text{Rec}},k^{*}_{\text{True}}}$ is the response matrix, $C_{\text{fit}}(k^{*}_{\text{True}})$ is the fit binned in k^{*}_{True}, and the denominator normal-
288 izes the result. Equation 9 describes that, for a given k^{*}_{Rec} bin, the observed value of $C(k^{*}_{\text{Rec}})$ is a weighted
289 average of all $C(k^{*}_{\text{True}})$ values, where the weights are the normalized number of counts in the [k^{*}_{Rec}, k^{*}_{True}
290] bin.

3.5 Non-Femtoscopic Background

292 A significant non-femtoscopic, non-flat, background is observed in all of the studied ΛK correlations at
293 large k^{*}. This background increases with decreasing centrality, is the same amongst all $\Lambda K^{\pm}$ pairs, and
294 is more pronounced in the ΛK^{0}_{S} system. This difference in $\Lambda K^{\pm}$ and ΛK^{0}_{S} backgrounds is due mainly to
295 the difference in kinematic cuts. It is suggested that this background effect is due primarily to particle
296 collimation associated with elliptic flow , and result from mixing events with unlike event-plane angles
297 [20]. The argument also suggests that the background should lead to an enhancement at low-k^{*}. An
298 attempt was made to decrease this background through the binning of events in Ψ_{EP}, but only a small
299 reduction in the signal was achieved due to the limited event-plane resolution.

300 The THERMINATOR 2 simulation has been shown to reproduce the background features in a πK anal-
301 ysis [20]. Figure 2 shows the THERMINATOR 2 simulation (open triangles) together with experimental

302 data (closed circles). The figure also shows a 6th-order polynomial fit to the simulation (dashed curves),
303 as well as the fit polynomial scaled to match the data (solid curves).

304 The description by THERMINATOR 2 of the non-femtoscopic backgrounds in the ΛK$^{\pm}$ systems is re-
305 markable, and can be used in a quantitative fashion to help fit the data. More specifically, the non-
306 femtoscopic backgrounds were modeled by (6th-order) polynomial fits to THERMINATOR 2 simulation
307 for the ΛK$^{\pm}$ analyses; one polynomial for each centrality class. The form of each polynomial was set
308 before use with the experimental data, by fitting to the THERMINATOR 2 simulation, shown in Fig. 2.
309 At the time of the fit, the polynomial used to correct each correlation function could only be adjust by
310 a simple scale factor to best match the data. The description of the ΛK^0_S is good at a qualitative level,
311 but not quantitatively good enough to be utilized in the fit. As such, a linear form is used to model the
312 background in the ΛK^0_S system. The background for each correlation function was fixed before use in the
313 signal region by fitting a linear form to the region $0.6 < k^* < 0.9$ GeV/c. In all cases, the non-femtoscopic
314 background correction was applied as a scale factor.
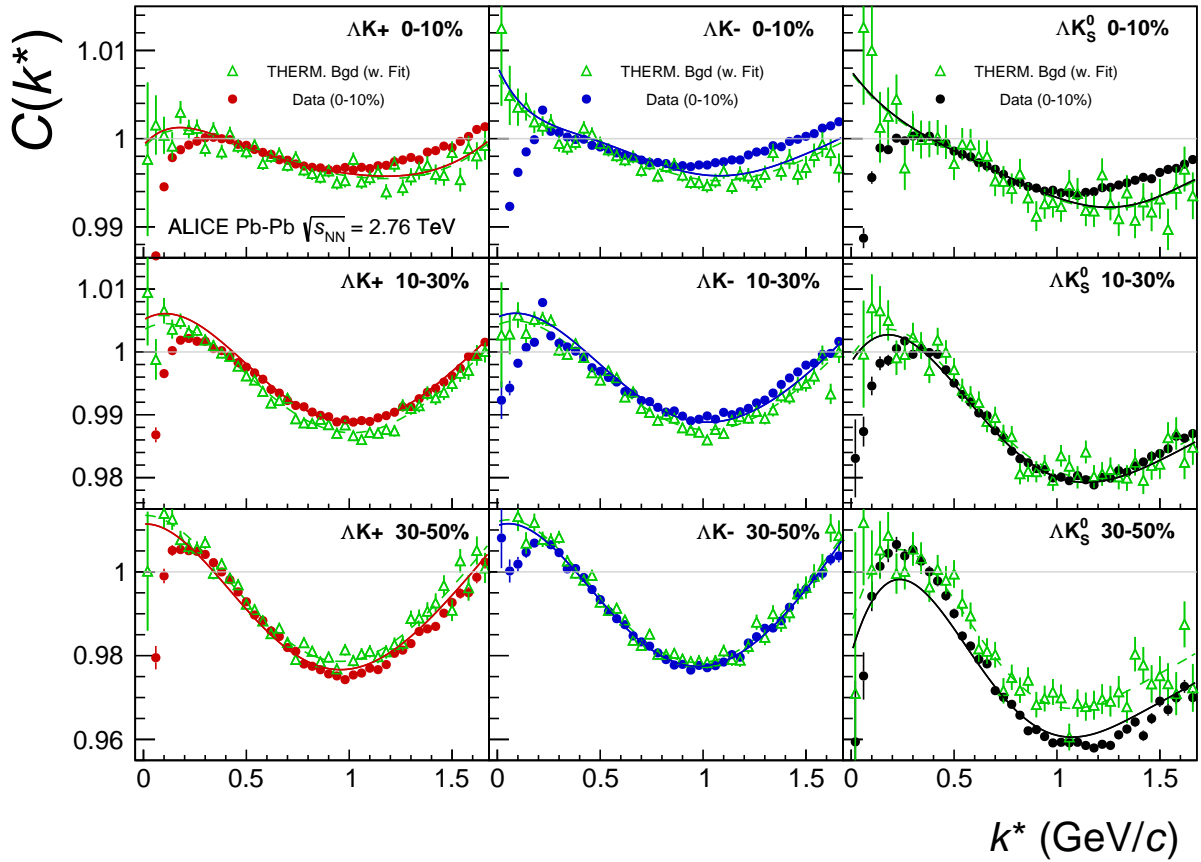
Fig. 2: (Color online) THERMINATOR 2 simulation (open triangles) together with experimental data (closed circles). Results are shown for ΛK$^+$ (left), ΛK$^-$ (middle), and ΛK^0_S (right). A 6th-order polynomial fit to the simulation is shown as a dashed curve. This polynomial is scaled to match the experimental data. The polynomial fit with scale factor applied is drawn as a solid curve.

315 An alternative approach to treating the non-femtoscopic background is to instead attempt to eliminate
316 it. The background may be effectively reduced by forming the reference distribution ($B(k^*)$) with the
317 "Stavinskiy method". With the Stavinskiy method, mixed-event pairs are not used for the reference
318 distribution; instead, same-event pseudo-pairs, formed by rotating one particle in a real pair by 180°
319 in the transverse plane, are used. This rotation rids the pairs of any femtoscopic correlation, while
320 maintaining correlations due to elliptic flow (and other suitably symmetric contributors). The effect on
321 the ΛK$^+$ correlation functions can be seen in the appendix, in Fig. A.1.

3.6 Summarized Fit Procedure

A simple χ^2 test is inappropriate for fitting correlation functions, as the ratio two Poisson distributions does not result in a Poisson distribution. Instead, a log-likelihood fit function is used as the statistic quantifying the quality of the fit [1]. The parameters of the fit are: λ_{Fit}, R, f_0 ($\Re f_0$ and $\Im f_0$ separately), d_0, and normalization N.

For the fit, a given pair and its conjugate (e.g. ΛK^+ and $\bar{\Lambda} K^-$) share scattering parameters ($\Re f_0$, $\Im f_0$, d_0), and the three distinct analyses (ΛK^+, ΛK^-, and ΛK^0_S) are assumed to have scattering parameters unique from each other. The pair emission source for a given centrality class is assumed similar between all analyses; therefore, for each centrality, all ΛK analyses share a common radius parameter. For each centrality class, a single λ_{Fit} parameter (see Eq. 6) is shared amongst all. Finally, each correlation function has a unique normalization parameter.

All correlation functions were normalized in the range $0.32 < k^* < 0.40$ GeV/c, and fit in the range $0.0 < k^* < 0.30$ GeV/c. For the ΛK^- analysis, the region $0.19 < k^* < 0.23$ GeV/c was excluded from the fit to exclude the bump caused by the Ω^- resonance. For each pair system, contributions from three residual contributors are accounted for, as discussed in Sec. 3.3, and whose individual λ values are listed in Table 4. Effects of finite track momentum resolution are also accounted for, as outlined in Sec. 3.4. The non-femtoscopic backgrounds are modeled using the THERMINATOR 2 simulation for the $\Lambda K^\pm$ analyses, and with a linear form for the ΛK^0_S system, as described in Sec. 3.5. In general, corrections are applied to the fit function.

To summarize, the complete fit function is constructed as follows:

1. The uncorrected, primary, correlation function, $C_{\Lambda K}(k^*_{\text{True}})$, is constructed using Eq. 5

2. The correlation functions describing the parent systems which contribute residually are obtained using:

    – Eq. 5 for the case of Coulomb-neutral pairs

    – $\Xi^- K^\pm$ experimental data for $\Xi^- K^\pm$ contributions

    – a Coulomb-only curve, with the help of Appendix B, for other pairs including the Coulomb interaction

3. The residual contributions to the ΛK correlation function is found by running each parent correlation function through the appropriate transform matrix, via Eq. 7

4. The primary and residual correlations are combined, via Eq. 6 with Tab. 4, to form $C'_{Fit}(k^*_{\text{True}})$

5. The correlation function is corrected to account for momentum resolution effects using Eq. 9, to obtain $C'_{\text{Fit}}(k^*_{\text{Rec}})$

6. Finally, the non-flat background correction, $F_{\text{Bgd}}(k^*_{\text{Rec}})$ is applied, and the final fit function is obtained, $C_{\text{Fit}}(k^*_{\text{Rec}}) = C'_{\text{Fit}}(k^*_{\text{Rec}}) * F_{\text{Bgd}}(k^*_{\text{Rec}})$

3.7 Systematic uncertainties

To quantify the systematic errors on the data, all correlation functions built using all varied cut values were bin-by-bin averaged, and the resulting variance of each bin was taken as the systematic error. The cuts included in the systematic study, as well as the values used in the variations, are shown in Tab. 5 (ΛK^0_S) and Tab. 6 ($\Lambda K^\pm$). Note, the central value corresponds to that used in the analysis.

Similarly, the fit parameters extracted from all of these correlation functions were averaged, and the resulting variances were taken as the systematic errors for the fit parameters. As with the systematic

13

363 errors on the data, this was performed for all varied cut values. Additionally, a systematic analysis
364 was done on the fit method through varying the k^* fit range, as well as varying the modeling of the
365 non-femtoscopic background. The choice of k^* fit range was varied by $\pm 25\%$. As previously stated,
366 the non-femtoscopic backgrounds are modeled using the THERMINATOR 2 simulation for the $\Lambda K^\pm$
367 analyses, and with a linear form for the ΛK^0_S system. To study the contribution of this choice to our
368 systematic errors, the backgrounds of all of the systems were modeled by fitting to the data with a with a
369 linear, quadratic, and Gaussian form. Additionally, the backgrounds of all systems were modeled with a
370 polynomial fit to the THERMINATOR simulation, scaled to match the data. The resulting uncertainties
371 in the extracted parameter sets were combined with the uncertainties arising from the particle and pair
372 cuts.

<div align="center">ΛK^0_S systematics</div>

DCA $\Lambda(\bar{\Lambda})$	4, 5, 6 mm
DCA K^0_S	2, 3, 4 mm
DCA $\Lambda(\bar{\Lambda})$ Daughters	3, 4, 5 mm
DCA K^0_S Daughters	2, 3, 4 mm
$\Lambda(\bar{\Lambda})$ Cosine of Pointing Angle	0.9992, 0.9993, 0.9994
K^0_S Cosine of Pointing Angle	0.9992, 0.9993, 0.9994
DCA to Primary Vertex of $p(\bar{p})$ Daughter of $\Lambda(\bar{\Lambda})$	0.5, 1, 2 mm
DCA to Primary Vertex of $\pi^-(\pi^+)$ Daughter of $\Lambda(\bar{\Lambda})$	2, 3, 4 mm
DCA to Primary Vertex of π^+ Daughter of K^0_S	2, 3, 4 mm
DCA to Primary Vertex of π^- Daughter of K^0_S	2, 3, 4 mm
Average Separation of Like-Charge Daughters	5, 6, 7 cm

Table 5: ΛK^0_S systematics

<div align="center">$\Lambda K^\pm$ systematics</div>

DCA $\Lambda(\bar{\Lambda})$	4, 5, 6 mm
DCA $\Lambda(\bar{\Lambda})$ Daughters	3, 4, 5 mm
$\Lambda(\bar{\Lambda})$ Cosine of Pointing Angle	0.9992, 0.9993, 0.9994
DCA to Primary Vertex of $p(\bar{p})$ Daughter of $\Lambda(\bar{\Lambda})$	0.5, 1, 2 mm
DCA to Primary Vertex of $\pi^-(\pi^+)$ Daughter of $\Lambda(\bar{\Lambda})$	2, 3, 4 mm
Average Separation of $\Lambda(\bar{\Lambda})$ Daughter with Same Charge as $K^\pm$	7, 8, 9 cm
Max. DCA to Primary Vertex in Transverse Plane of $K^\pm$	1.92, 2.4, 2.88
Max. DCA to Primary Vertex in Longitudinal Direction of $K^\pm$	2.4, 3.0, 3.6

Table 6: $\Lambda K^\pm$ systematics

4 Results

374 Figures 3–5 show the ΛK data with fits for all studied centrality bins (0–10%, 10–30%, and 30–50%).
375 All analyses were fit simultaneously across all centralities, with a single radius and normalization λ_{Fit} pa-
376 rameter for each centrality bin. Scattering parameters ($\Re f_0$, $\Im f_0$, d_0) were shared between pair-conjugate
377 systems, but assumed unique between the different ΛK charge combinations (i.e. a parameter set describ-
378 ing the ΛK^+ & $\bar{\Lambda} K^-$ system, a second set describing the ΛK^- & $\bar{\Lambda} K^+$ system, and a third for the ΛK^0_S
379 & $\bar{\Lambda} K^0_S$ system). Each correlation function received a unique normalization parameter. The fits were

corrected for finite momentum resolution effects, non-femtoscopic backgrounds, and residual correla-
tions resulting from the feed-down from resonances. In Figs. 3–5, lines represent statistical errors, while
boxes represent systematic errors. The dotted curve shows the primary (ΛK) contribution to the fit (i.e.
$1 + \lambda'_{\Lambda K} C_{\Lambda K}(k^*_{\Lambda K})$ in Eq. 6), the dashed curve shows the fit to the non-femtoscopic background (with a
polynomial fit to the THERMINATOR 2 simulation for the $\Lambda K^\pm$ systems, and a linear form fit to the
data for the ΛK^0_S), and the solid curve shows the final fit after all corrections have been applied.
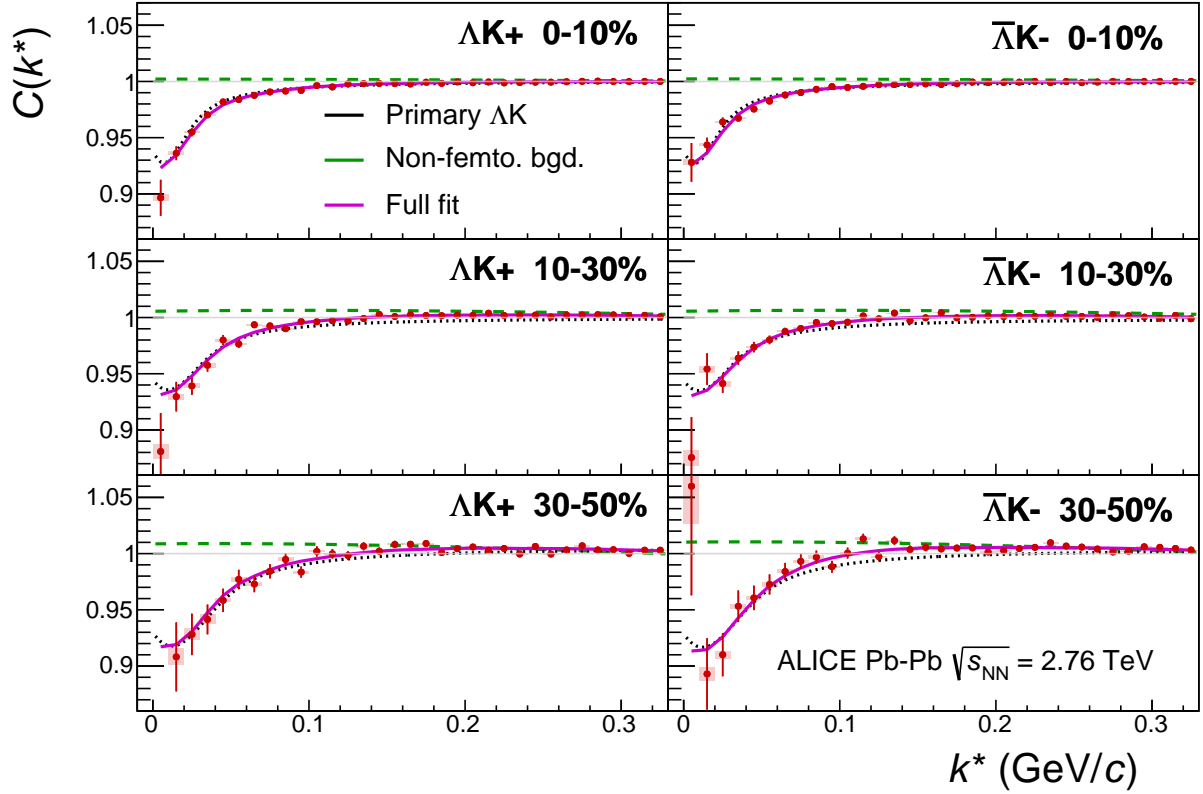
Fig. 3: (Color online) Fit results for the ΛK^+ and $\bar{\Lambda} K^-$ data. The ΛK^+ data is shown in the left column, the $\bar{\Lambda} K^-$
in the right, and the rows differentiate the different centrality bins (0–10% in the top, 10–30% in the middle, and
30–50% in the bottom). See text for further details.

Figure 6 summarizes well the results of the present study. In the summary plot, the extracted scattering
parameters are shown in the form of a $\Im f_0$ vs $\Re f_0$ plot, which includes the d_0 values to the right side.
Also shown are the λ vs. radius parameters for all three studied centrality bins. In addition to the results
of this study, theoretical predictions made using chiral perturbation theory [21, 22] are shown.

For all studied systems, a positive imaginary part, $\Im(f_0)$, of the scattering lengths are extracted. This is
expected, as $\Im(f_0)$ describes the inelastic scattering channels. More interestingly, the results show that
the ΛK^+ and ΛK^- systems differ in the sign of the real part, $\Re(f_0)$, of their scattering lengths, with a
negative value for ΛK^+ and positive value for ΛK^-. The $\Re f_0$ extracted for the ΛK^0_S system is positive,
and within errors of that of the ΛK^-. The real part of the scattering length describes the effect of the
strong interaction, making the difference in these systems quite intriguing. A positive $\Re(f_0)$ (ΛK^-,
ΛK^0_S) signifies that the effect of the strong force is attractive, while a negative $\Re(f_0)$ (ΛK^+) signifies
a repulsion. Past studies of kaon-proton scattering found the K$^-$-p interaction to be attractive, and that
of the K$^+$-p to be repulsive [2–4]. With respect to the kaons, this is similar to the current finding of an
attractive Λ-K$^-$ interaction and a repulsive Λ-K$^+$ interaction. This difference could be due to an effect
arising from different quark-antiquark interactions between the pairs (s$\bar{\text{s}}$ in ΛK^+, u$\bar{\text{u}}$ in ΛK^-). A related
explanation could be that the effect is due to the different net strangeness for each system.

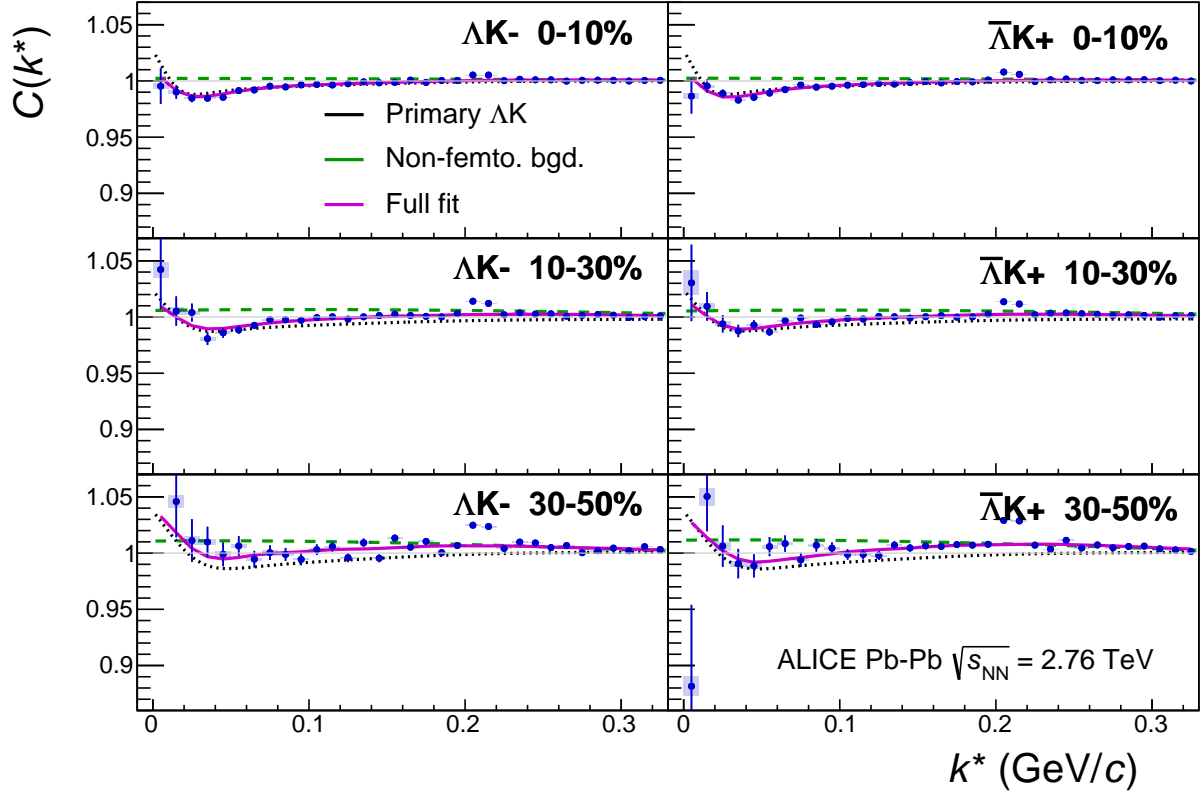**Fig. 4:** (Color online) Fit results for the ΛK^- and $\bar{\Lambda} K^+$ data. The ΛK^- data is shown in the left column, the $\bar{\Lambda} K^+$ in the right, and the rows differentiate the different centrality bins (0–10% in the top, 10–30% in the middle, and 30–50% in the bottom). See text for further details.

402 A comparison of the extracted radii from this study to those of other systems measure by ALICE [23] is
403 shown in Figure 7. The figure shows extracted R_{inv} vs. m_{T} for several centralities and for several different
404 systems. The m_{T} value used for the present ΛK results was taken as the average of the three systems[1].
405 The radii are observed to increase for more central events, as expected from a simple geometric picture of
406 the collisions. They also demonstrate a decreasing size with increasing m_{T}, as expected in the presence of
407 collective radial flow [24]. It was found that [25], even in the presence of good global m_{T}-scaling for the
408 three-dimensional radii in the Longitudinally Co-Moving System (LCMS), a particle species dependence
409 will exist for the R_{inv} measured in the Pair Rest Frame (PRF), due to trivial kinematic reasons. These
410 kinematic effects, resulting from the transformation from LCMS to PRF, causes smaller masses to exhibit
411 larger R_{inv} [23] (explaining, for instance, how the pion radii are systematically higher than kaon radii at
412 the same approximate m_{T}).

413 It is clear from the results in Fig. 7 that the ΛK systems do not conform to the approximate m_{T}-scaling
414 of the identical particle pair source sizes. At first thought, this may appear to be a troubling result; the
415 approximate scaling is an observed consequence of the collective behavior of the soft (low-p_{T}) sector
416 of the produced system. The Λ and K particles certainly participate in the collective expansion of the

---

[1] For non-identical particle pairs, to be more directly analogous to the single particle m_{T}, the definition of the pair transverse mass used in this study is

$$m_{\mathrm{T,pair}}^2 = \left(\frac{m_{\mathrm{inv}}}{2}\right)^2 + \left(\frac{1}{2}|\boldsymbol{p}_{\mathrm{T,1}} + \boldsymbol{p}_{\mathrm{T,2}}|\right)^2$$
$$= (K^0)^2 - (K^3)^2$$
$$\text{where } K^\mu \equiv \frac{1}{2}\left(p_1^\mu + p_2^\mu\right)$$

16
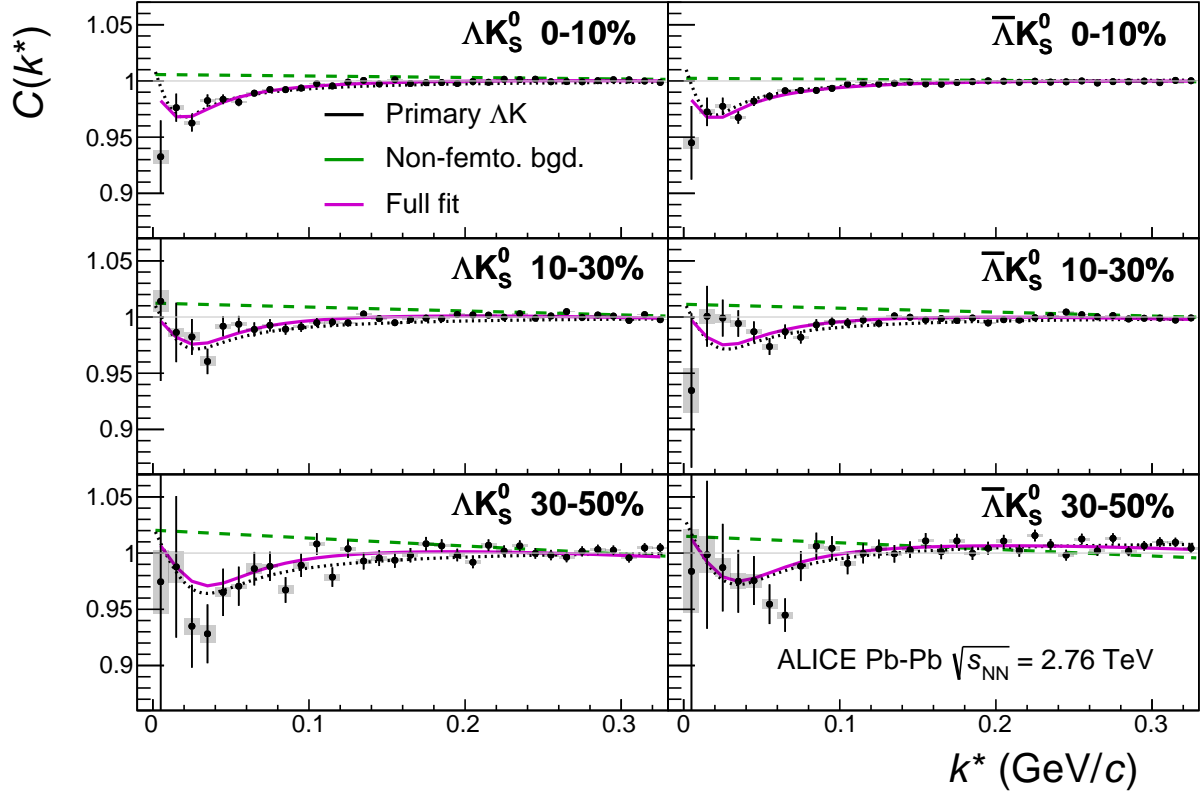
Fig. 5: (Color online) Fit results for the ΛK_S^0 and $\bar{\Lambda} K_S^0$ data. The ΛK_S^0 data is shown in the left column, the $\bar{\Lambda} K_S^0$ in the right, and the rows differentiate the different centrality bins (0–10% in the top, 10–30% in the middle, and 30–50% in the bottom). See text for further details.

QGP medium, but, importantly, they are non-identical particles, and all other systems in Fig. 7 contain identical particles. In the case of identical particle femtoscopy, the pair source is comprised of two identical single particle sources, and the pair source size extracted is simply a factor $\sqrt{2}$ larger than those single particle sources. Thus, the identical particle pair source radii naturally follow the single particle source m_T-scaling in a simple manner.

When dealing with non-identical particles, the pair emission source, which is measured by femtoscopy, is the superposition of two single-particle sources. The hydrodynamic nature of the medium produces the approximate m_T-scaling with respect to these single-particle sources, not the pair sources. More specifically, the hydrodynamic response of the system confines higher-m_T particles to smaller homogeneity regions, also pushes their average emission points further in the "out" direction [26]. Therefore, it is expected that the Λ source is both smaller in size and further out in the fireball than that of the kaons. The combination of two unique sources separated in space-time, when probing correlations between non-identical particle pairs, can lead to extracted radii falling outside of the (identical particle femtoscopy) m_T-scaling trend.

It is well established that non-identical particle femtoscopic studies are able to probe deeper than the second moments of the pair distribution functions accessed via identical particle studies. In addition to this, non-identical particle studies are able to measure the relative emission shifts, the first moments of the emission function [27]. For the study of ΛK pairs at mid-rapidity in Pb-Pb collisions, a separation of the single-particle sources in the out direction is expected. One elegant method for extracting information about the emission asymmetries is via a spherical decomposition of the correlation function. With this method, one can draw a wealth of information from just a few components of the decomposition. Particularly, the C_{00} component is similar to the 1D correlation functions typically studied, and probes the
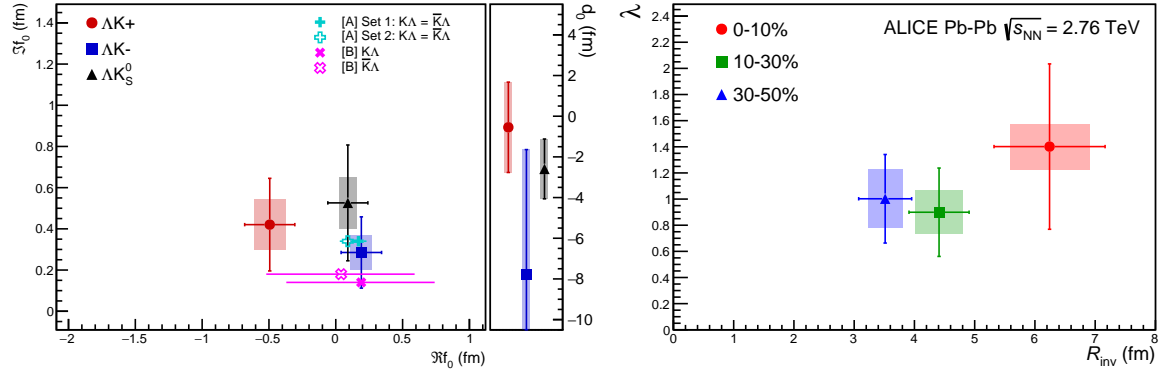
Fig. 6: (Color online) Extracted fit parameters for all of the ΛK systems. [Left]: $\Im f_0$ vs. $\Re f_0$, together with d_0 to the right for the ΛK^+ (circles), ΛK^- (squares) and ΛK_S^0 (triangles) systems. [Right]: λ vs. Radius for the 0–10% (circles), 10–30% (squares), and 30–50% (triangles) centrality bins. In the fit, all ΛK systems share common radii. The cross ([A] = Ref. [21]) and X symbols ([B] = Ref. [22]) points show theoretical predictions made using chiral perturbation theory.
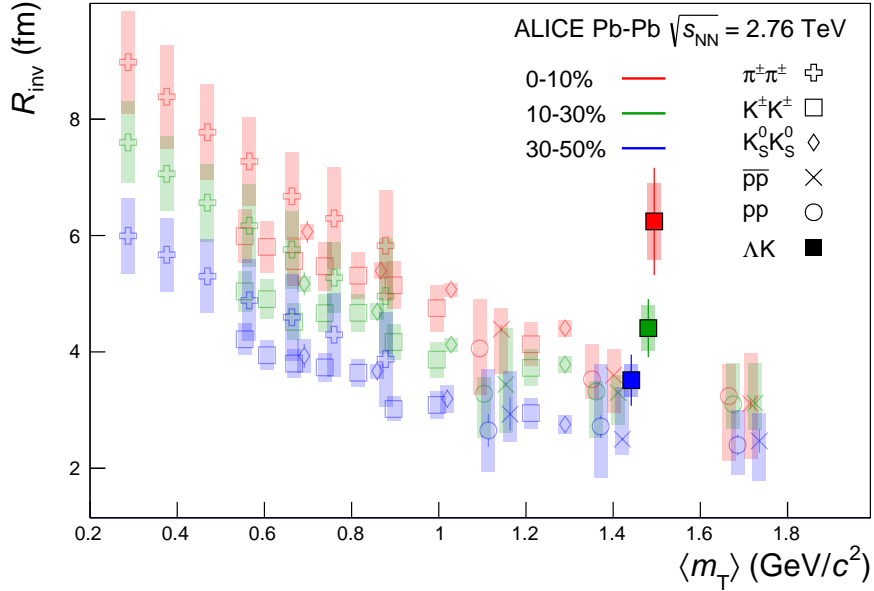
Fig. 7: (Color online) Extracted fit R_{inv} parameters as a function of pair transverse mass (m_T) for various pair systems over several centralities. The ALICE published data [23] is shown with transparent, open symbols.

overall size of the source. The $\Re C_{11}$ component probes the asymmetry of the system in the out direction; a non-zero value reveals the asymmetry.

Figure 8 shows the C_{00} and $\Re C_{11}$ components from the spherical decomposition of the ΛK^+ data in the 0–10% centrality bin. The $\Re C_{11}$ component shows a clear deviation from zero, and the negative value signifies that the Λ particles are, on average, emitted further out and/or earlier than the K mesons. This effect is supported by the results obtained from the THERMINATOR 2 model, shown in Fig. C.1. The effect of a non-zero shift in the source will naturally lead to larger measured radii. This is intuitive, and also reaffirmed in the simulation with THERMINATOR 2 shown in App. C. Larger effective radii are also found to result from inserting a Gaussian source with a non-zero shift into the Koonin-Pratt equation and numerically integrating.

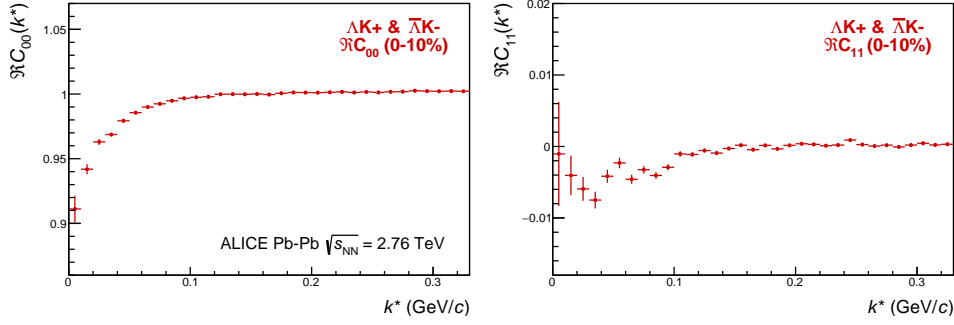It should be emphasized that the extracted ΛK source sizes do not indicate any sort of contradiction with

18

Fig. 8: (Color online) C_{00} (left) and $\Re C_{11}$ (right) components of a spherical harmonic decomposition of the ΛK^+ correlation function for the 0–10% centrality bin. The C_{00} component is similar to the 1D correlation functions typically studied, and probes the overall size of the source. The $\Re C_{11}$ component probes the asymmetry in the system; a non-zero value reveals the asymmetry

450 the hydrodynamic nature of the system dictating the substructure of the femtoscopic radii. The results,
451 rather, support this picture. As described above, the hydrodynamic response of the system confines
452 the Λ emission to smaller homogeneity regions located further out in the fireball, as compared to the
453 kaons. Therefore, the single particle Λ and K source sizes differ both in size and space-time location.
454 When studying these pairs under the assumption of a spherically symmetric Gaussian source with no
455 offset in the "out" direction, this can lead to larger extracted radii, as demonstrated above with the
456 THERMINATOR 2 simulation.

5 Summary

458 Results from a femtoscopic analysis of ΛK correlations in Pb-Pb collisions at $\sqrt{s_{\mathrm{NN}}}$ = 2.76 TeV with
459 ALICE at the LHC have been presented. The femtoscopic radii, λ parameters, and scattering parameters
460 were extracted from one-dimensional correlation functions in terms of the invariant momentum differ-
461 ence. The scattering parameters of ΛK pairs in all three charge combinations (ΛK^+, ΛK^-, and ΛK_S^0)
462 have been measured for the first time. A striking difference in the ΛK^+ and ΛK^- correlation functions
463 is observed, which is reflected in the unique set of scattering parameters extracted for each. The ΛK_S^0
464 systems is somewhat intermediate to these two cases. The ΛK^+ systems exhibits a negative $\Re(f_0)$, while
465 those extracted from the ΛK^- and ΛK_S^0 systems are positive. This implies that the strong interaction is
466 repulsive for the ΛK^+ system and attractive for ΛK^- and ΛK_S^0. The physics underlying this phenomenon
467 is currently not well understood, but this could be due to different quark-antiquark interactions between
468 the pairs, or from different net strangeness for each system. The non-femtoscopic background is found
469 to result almost entirely from collective effects, and is described quantitatively with unprecedented pre-
470 cision with the THERMINATOR 2 event generator. Finally, the ΛK systems exhibit source radii larger
471 than expected from extrapolation from identical particle femtoscopic studies. This effect is interpreted
472 as resulting from the separation in space-time of the single-particle Λ and K source distributions.

Acknowledgements

References

475 [1] M. A. Lisa, S. Pratt, R. Soltz, and U. Wiedemann, "Femtoscopy in relativistic heavy ion
476   collisions," *Ann. Rev. Nucl. Part. Sci.* **55** (2005) 357–402, `arXiv:nucl-ex/0505014`
477   `[nucl-ex]`.

478 [2] W. E. Humphrey and R. R. Ross, "Low-Energy Interactions of K- Mesons in Hydrogen," *Phys.*
479   *Rev.* **127** (1962) 1305–1323.

[3] D. Hadjimichef, J. Haidenbauer, and G. Krein, "Short range repulsion and isospin dependence in the KN system," *Phys. Rev.* **C66** (2002) 055214, arXiv:nucl-th/0209026 [nucl-th].

[4] Y. Ikeda, T. Hyodo, and W. Weise, "Chiral SU(3) theory of antikaon-nucleon interactions with improved threshold constraints," *Nucl. Phys.* **A881** (2012) 98–114, arXiv:1201.6549 [nucl-th].

[5] R. Lednický and V. L. Lyuboshitz, "Final State Interaction Effect on Pairing Correlations Between Particles with Small Relative Momenta," *Sov. J. Nucl. Phys.* **35** (1982) 770. [Yad. Fiz.35,1316(1981)].

[6] **ALICE** Collaboration, K. Aamodt *et al.*, "The alice experiment at the cern lhc," *JINST* **3** (2008) S08002. http://stacks.iop.org/1748-0221/3/i=08/a=S08002.

[7] **ALICE** Collaboration, B. Abelev *et al.*, "Centrality determination of Pb-Pb collisions at $\sqrt{s_{NN}} =$ 2.76 TeV with ALICE," *Phys. Rev.* **C88** no. 4, (2013) 044909, arXiv:1301.4361 [nucl-ex].

[8] J. Alme *et al.*, "The ALICE TPC, a large 3-dimensional tracking device with fast readout for ultra-high multiplicity events," *Nucl. Instrum. Meth. A* **622** (2010) 316–367, arXiv:1001.1950 [physics.ins-det].

[9] B. A. et al and T. A. Collaboration, "Technical Design Report for the Upgrade of the ALICE Inner Tracking System," *Journal of Physics G: Nuclear and Particle Physics* **41** no. 8, (2014) 087002. http://stacks.iop.org/0954-3899/41/i=8/a=087002.

[10] **ALICE** Collaboration, B. B. Abelev *et al.*, "Performance of the ALICE Experiment at the CERN LHC," *Int. J. Mod. Phys.* **A29** (2014) 1430044, arXiv:1402.4476 [nucl-ex].

[11] A. Akindinov *et al.*, "Performance of the ALICE Time-Of-Flight detector at the LHC," *Eur. Phys. J. Plus* **128** (2013) 44.

[12] X.-N. Wang and M. Gyulassy, "HIJING: A Monte Carlo model for multiple jet production in pp, pA, and AA collisions," *Phys. Rev. D* **44** (Dec, 1991) 3501–3516. https://link.aps.org/doi/10.1103/PhysRevD.44.3501.

[13] R. Brun, F. Bruyant, F. Carminati, S. Giani, M. Maire, A. McPherson, G. Patrick, and L. Urban, "GEANT Detector Description and Simulation Tool,".

[14] **ALICE** Collaboration, S. Acharya *et al.*, "Kaon femtoscopy in Pb-Pb collisions at $\sqrt{s_{NN}} = 2.76$ TeV," *Phys. Rev.* **C96** no. 6, (2017) 064613, arXiv:1709.01731 [nucl-ex].

[15] **Particle Data Group** Collaboration, C. Patrignani *et al.*, "Review of Particle Physics," *Chin. Phys.* **C40** no. 10, (2016) 100001.

[16] S. E. Koonin, "Proton Pictures of High-Energy Nuclear Collisions," *Phys. Lett.* **B70** (1977) 43–47.

[17] S. Pratt, T. Csorgo, and J. Zimanyi, "Detailed predictions for two pion correlations in ultrarelativistic heavy ion collisions," *Phys. Rev.* **C42** (1990) 2646–2652.

[18] G. I. Kopylov, "Like particle correlations as a tool to study the multiple production mechanism," *Phys. Lett.* **B50** (1974) 472–474. [,39(1974)].

[19] M. Chojnacki, A. Kisiel, W. Florkowski, and W. Broniowski, "THERMINATOR 2: THERMal heavy IoN generATOR 2," *Comput. Phys. Commun.* **183** (2012) 746–773, arXiv:1102.0273 [nucl-th].

[20] A. Kisiel, "Non-identical particle correlation analysis in the presence of non-femtoscopic correlations," *Acta Physica Polonica B* **48** (04, 2017) 717.

[21] Y.-R. Liu and S.-L. Zhu, "Meson-baryon scattering lengths in HB chi PT," *Phys. Rev.* **D75** (2007) 034003, arXiv:hep-ph/0607100 [hep-ph].

[22] M. Mai, P. C. Bruns, B. Kubis, and U.-G. Meissner, "Aspects of meson-baryon scattering in three and two-flavor chiral perturbation theory," *Phys. Rev.* **D80** (2009) 094006, arXiv:0905.2810 [hep-ph].

[23] **ALICE** Collaboration, J. Adam *et al.*, "One-dimensional pion, kaon, and proton femtoscopy in Pb-Pb collisions at $\sqrt{s_{NN}}$ =2.76 TeV," *Phys. Rev.* **C92** no. 5, (2015) 054908, arXiv:1506.07884 [nucl-ex].

[24] S. V. Akkelin and Yu. M. Sinyukov, "The HBT interferometry of expanding sources," *Phys. Lett.* **B356** (1995) 525–530.

[25] A. Kisiel, M. Gaayn, and P. Boek, "Pion, kaon, and proton femtoscopy in Pb–Pb collisions at $\sqrt{s_{NN}}$=2.76 TeV modeled in (3+1)D hydrodynamics," *Phys. Rev.* **C90** no. 6, (2014) 064914, arXiv:1409.4571 [nucl-th].

[26] F. Retiere and M. A. Lisa, "Observable implications of geometrical and dynamical aspects of freeze out in heavy ion collisions," *Phys. Rev.* **C70** (2004) 044907, arXiv:nucl-th/0312024 [nucl-th].

[27] A. Kisiel, "Non-identical particle femtoscopy at $\sqrt{s_{NN}} = 200$ GeV in hydrodynamics with statistical hadronization," *Phys. Rev.* **C81** (2010) 064906, arXiv:0909.5349 [nucl-th].

[28] A. Stavinskiy *et al.*, "Some new aspects of femtoscopy at high energy," *Nukleonika* **49** (**Supplement 2**) (2004) S23.

[29] R. Lednický, "Finite-size effects on two-particle production in continuous and discrete spectrum," *Phys. Part. Nucl.* **40** (2009) 307–352, arXiv:nucl-th/0501065 [nucl-th].

A   Stavinskiy Reference Method

Another option for obtaining the reference distribution, $B(k^*)$, is to use, what will be referred to as, the "Stavinskiy method" [28]. The method was first proposed to handle the case of one event femtoscopy, and has been suggested for use in eliminating momentum conservation effects in the reference distribution [1]. The method is appropriate for collisions between symmetric projectiles, at sufficiently large energy, with a detector which is symmetrical with respect to the transition $\mathbf{r} \to -\mathbf{r}$. The purpose of using the Stavinskiy method in this ΛK analysis is to rid the correlation functions of the non-femtoscopic background. More specifically, the intent is to handle background contributions from elliptic flow, and other sources having reflection symmetry in the transverse plane. With the Stavinskiy method, mixed-event pairs are not used for the reference distribution; instead, same-event pseudo-pairs, formed by rotating one particle in a real pair by $180°$ in the transverse plane, are used. This rotation rids the pairs of any femtoscopic correlation, while maintaining correlations due to elliptic flow (and other suitably symmetric contributors). The results of correctly implementing such a procedure are shown in Figure A.1. The figure shows the Stavinskiy method does a very good job of ridding the ΛK^+ correlations of their non-femtoscopic backgrounds.

Now, one must be somewhat careful when applying this Stavinskiy method. To obtain correct results, the pseudo-pairs must be run through the same pair cuts used for the real pairs in the analyses. In an ideal world, the pair cut would only remove truly bad pairs results from splitting, merging, etc. In the real world, the pair cut always throws out some of the good with the bad. For the pseudo-pairs to form a reliable reference, they too must experience the pair cut, and the loss of "good" pseudo-pairs. This issue affected mainly the ΛK^+ & $\bar{\Lambda} K^-$ system in this analysis.

B   Strong and Coulomb Fitter

When modeling systems which include both strong and Coulomb effects, Eq. 5 is no longer valid, and, in fact, there is no analytical form with which to fit. To solve such a problem, and to fit such a system, one must develop a more fundamental model, beginning with Eq. 2 and using the two-particle wave-function including both strong and Coulomb interactions [29]:

$$\Psi_{\mathbf{k}^*}(\mathbf{r}^*) = e^{i\delta_c}\sqrt{A_c(\eta)}[e^{i\mathbf{k}^* \cdot \mathbf{r}^*}F(-i\eta, 1, i\xi) + f_c(k^*)\frac{\tilde{G}(\rho,\eta)}{r^*}] \tag{B.1}$$

where $\rho = k^*r^*$, $\eta = (k^*a_c)^{-1}$, $\xi = \mathbf{k}^* \cdot \mathbf{r}^* + k^*r^* \equiv \rho(1 + \cos\theta^*)$, and $a_c = (\mu z_1 z_2 e^2)^{-1}$ is the two-particle Bohr radius (including the sign of the interaction). δ_c is the Coulomb s-wave phase shift, $A_c(\eta)$ is the Coulomb penetration factor, $\tilde{G} = \sqrt{A_c}(G_0 + iF_0)$ is a combination of the regular (F_0) and singular (G_0) s-wave Coulomb functions. $f_c(k^*)$ is the s-wave scattering amplitude:

$$f_c(k^*) = [\frac{1}{f_0} + \frac{1}{2}d_0k^{*2} - \frac{2}{a_c}h(\eta) - ik^*A_c(\eta)]^{-1} \tag{B.2}$$

where, the "h-function", $h(\eta)$, is expressed through the digamma function, $\psi(z) = \Gamma'(z)/\Gamma(z)$ as:

$$h(\eta) = 0.5[\psi(i\eta) + \psi(-i\eta) - \ln(\eta^2)] \tag{B.3}$$

In this case, the λ parameter may be included as:

$$C(\mathbf{k}^*) = (1-\lambda) + \lambda \int S(\mathbf{r}^*)|\Psi^S_{\mathbf{k}^*}(\mathbf{r}^*)|^2 d^3\mathbf{r}^* \tag{B.4}$$
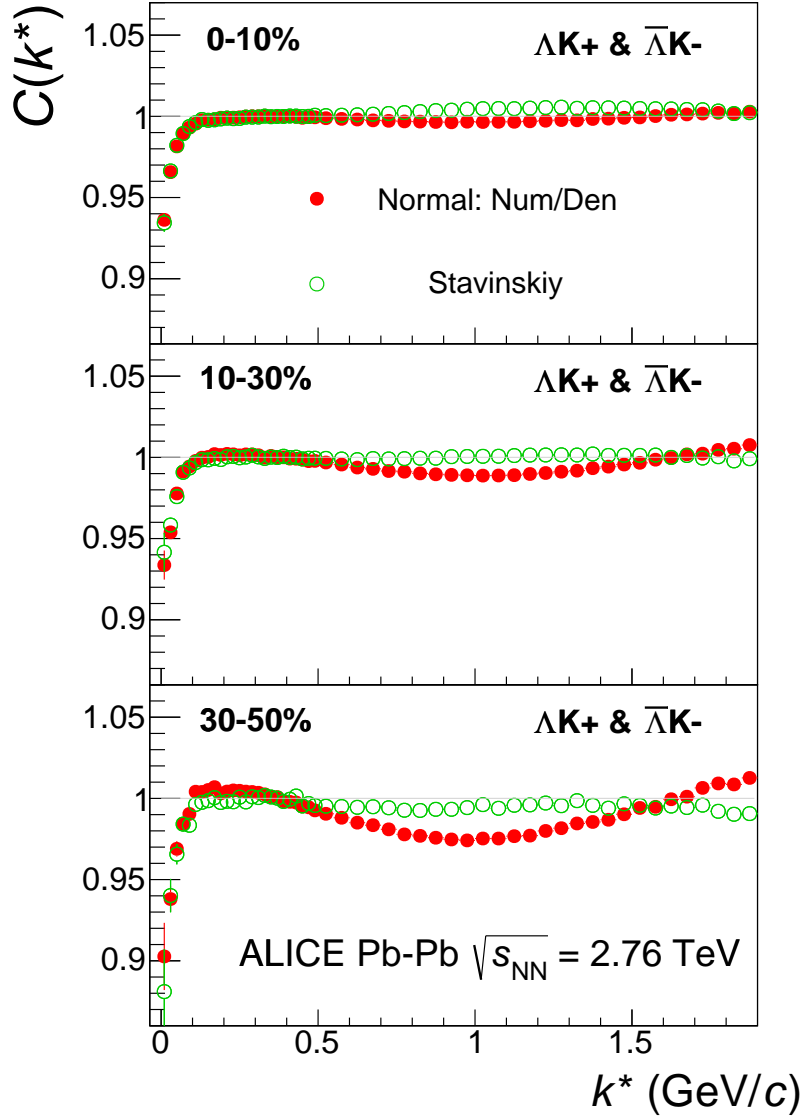
Fig. A.1: (Color online) $\Lambda K^+(\bar{\Lambda}K^-)$ correlation functions built using the Stavinskiy method for 0–10%, 10–30%, and 30–50% centralities. Closed symbols represent correlations built using the normal mixed-event reference distribution, while open symbols represent correlations formed using the Stavinskiy same-event pseudo-pairs as a reference.

To build a fit function for a system including both strong and Coulomb interactions two related options were considered. The first option was to numerically integrate Eq. 2. The second option was to simulate a large sample of particle pairs, calculate the wave function describing the interaction, and average to obtain the integral in Eq. 2. In either case, the solution would involve some very complicated mathematical functions, as can be seen in Eqs. B.1 to B.3. Having no experience with either of these options, we elected the latter of simulating pairs.

C Relative Emission Shifts with THERMINATOR 2

Fig. C.1 shows results from the THERMINATOR 2 event generator for an impact parameter of b = 2 fm. As THERMINATOR does not include any final state effects, the femtoscopic correlation was introduced by assuming a set of scattering parameters $(\Re f_0, \Im f_0, d_0) = (-1.16, 0.51, 1.08)$ and weighting the signal distribution (numerator pairs) with the modulus squared of the two-particle wave function, $|\Psi|^2$.

The top left of Fig. C.1(a) shows a fit to the one-dimensional correlation function from THERMINATOR 2. The scattering parameters are known precisely here, as they served as the weights used in the simulation, and are kept constant in the fit. Only the extracted one-dimensional source size is of interest here, so the λ parameter is also fixed at unity. The other three plots in Fig. C.1(a) show the source distribution in the out (top right), side (bottom left), and long (bottom right) directions (all in the PRF). The source distributions have all been fitted with a Gaussian form, the result of which is printed within the respective plot. One immediately sees a significant shift in the out direction, $\mu_{\mathrm{out}} \approx 4$ fm, and negligible shift in the other two directions, $\mu_{\mathrm{side}} \approx \mu_{\mathrm{long}} \approx 0$ fm. The figure demonstrates that, within the THERMINATOR 2 model, the Λ is, on average, emitted further out that its K partner. Finally, Fig. C.1(b) shows the distribution of the relative time of emittance, again in the PRF. The figure shows that the Λ is, on average, emitted earlier than its K partner.

This section concludes with a brief look at how a spatial separation of the single particle sources affects the radii extracted from a femtoscopic analysis. To achieve this, THERMINATOR 2 is used in a similar fashion as described above, but with one important difference. Instead of taking the source information from THERMINATOR 2, the source is drawn from a pre-determined Gaussian distribution. In all cases, $R_{\mathrm{out}} = R_{\mathrm{side}} = R_{\mathrm{long}} = 5$ fm, and $\mu_{\mathrm{side}} = \mu_{\mathrm{long}} = 0$ fm. In Figure C.2, results are shown for the case of $\mu_{out} = 1$ fm, $\mu_{out} = 3$ fm, and $\mu_{out} = 6$ fm. In this figure, the side and long distributions are not shown, as they are simple Gaussians of width 5 fm centered about the origin. The figure demonstrates that as the separation μ_{out} increases, so do the extracted femtoscopic radii.
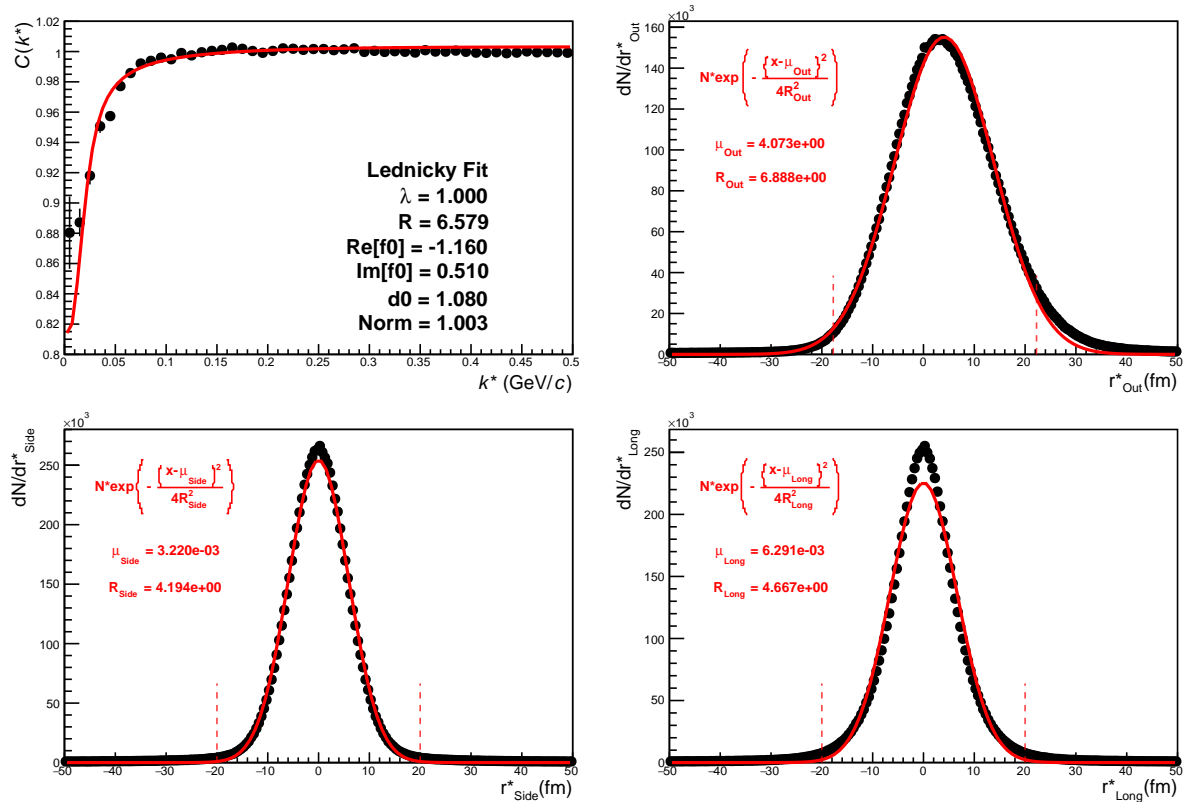
(a) (Top Left) Simple fit on simulation from THERMINATOR 2. Generated source in the (Top Right) out, (Bottom Left) side, and (Bottom Right) long directions.
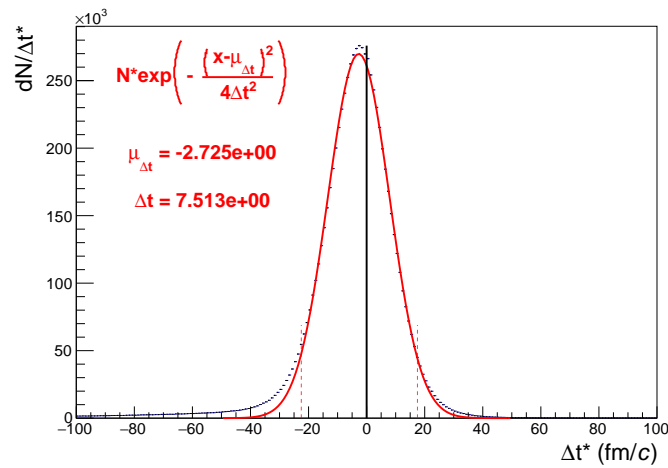
(b) Temporal characteristics of the source.

Fig. C.1: (Color online) Extracted radius when performing a simple fit on simulation from THERMINATOR 2, along with the spatio-temporal characteristics generated by the simulation.
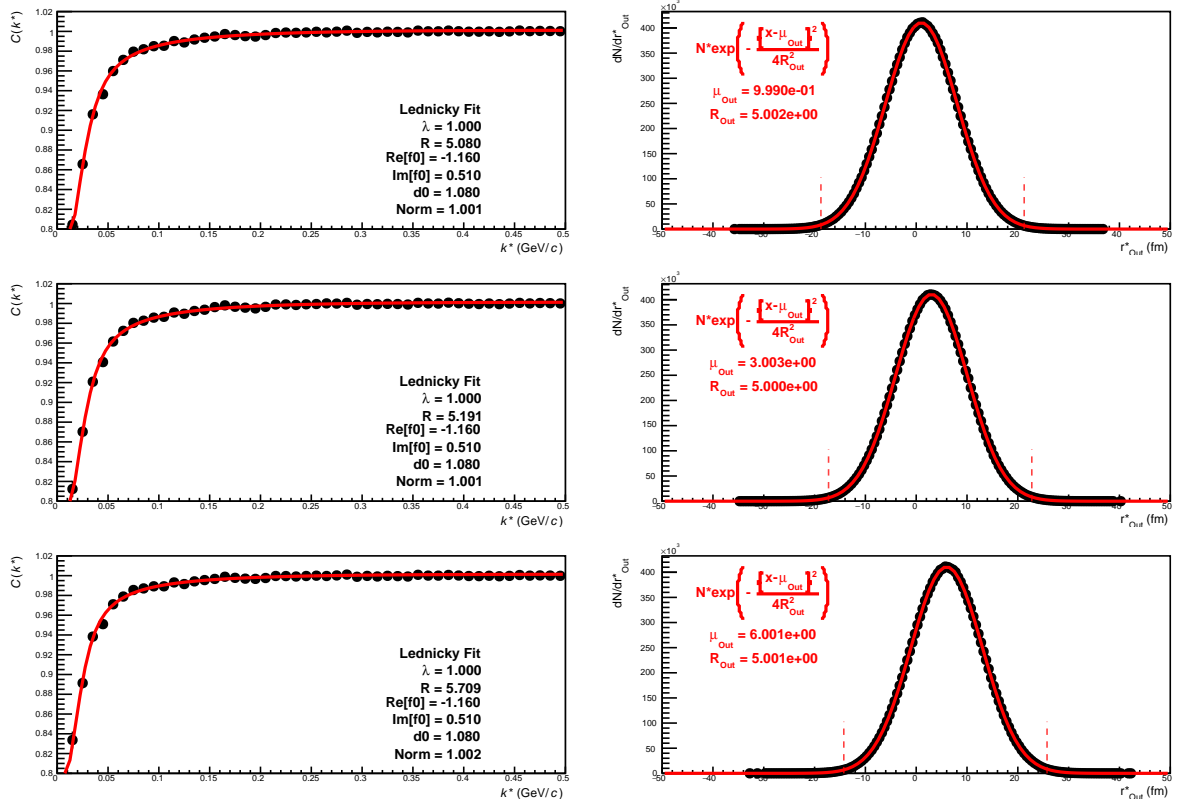
Fig. C.2: (Color online) Probing the effect of varying the source shift in the outward direction, μ_{Out}, within the THERMINATOR 2 framework. To achieve this, particle pairs are formed from the simulation, but with altered spatial characteristics achieved by drawing the out, side, and long components from pre-determined Gaussian distributions. The plots on the left show fits resulting from the sources (in the out direction) shown on the right. The sources in the side and long directions are not shown, and are both Gaussians of width 5 fm centered at the origin for all cases. Moving from top to bottom, μ_{Out} increase from 0 to 6 fm, the effect of which clearly increases the effective radius extracted in the fit.

605 **D The ALICE Collaboration**